IEEE Access
Multidisciplinary ⋮ Rapid Review ⋮ Open Access Journal

Received 26 January 2024, accepted 9 February 2024, date of publication 21 February 2024, date of current version 29 February 2024.

Digital Object Identifier 10.1109/ACCESS.2024.3368799

RESEARCH ARTICLE

Single-Loop Robust Decoupling Control Base on Perturbation Estimation for DC-Based DFIG

YULIANG SUN[1], JINGWEI YANG[2], AND ZHONGCAI ZHANG[1,3], (Member, IEEE)
[1]School of Engineering, Qufu Normal University, Rizhao 276827, China
[2]Department of Information Engineering, Shandong Water Conservancy Vocational College, Rizhao 276827, China
[3]School of Artificial Intelligence, Nankai University, Tianjin 300350, China

Corresponding author: Yuliang Sun (shuibeizi@163.com)

This work was supported in part by the Natural Science Foundation of China under Grant 62173207, in part by the Natural Science Foundation of Shandong Province under Grant ZR2023MF113, in part by the Postdoctoral Science Special Foundation under Grant 2023T160334, in part by the Youth Innovation Team Project of Colleges and Universities in Shandong Province under Grant 2022KJ176, and in part by the Graduate Teaching Case Base Project of Shandong Province under Grant SDYAL20109.

ABSTRACT This paper presents a perturbation observer based single-loop robust decoupling control scheme (RDC-PO) for DC-based DFIG with dual voltage source converters to enhance maximum power point tracking (MPPT) and improve fault-ride-through (FRT) capability. The unknown nonlinear effects caused by aerodynamic and modeling uncertainties are aggregated into a perturbation term, which is estimated by a sliding-mode perturbation observer. Then, a single-loop linear feedback controller with no intermediate link is designed to quickly compensate disturbance estimation in real time. Furthermore, the control algorithm does not necessitate a precise DFIG model. Additionally, the incorporation of nonlinear robust control compensates for the inherent limitations of linear control, thereby endowing the proposed control algorithm with the advantages of facile implementation akin to traditional linear control and global consistency characteristic of nonlinear robust control. Simulation results show that RDC-PO has superior transient and steady-state performance compared with double-loop feedback controller (DFC) and single-loop feedback control (SFC) in MPPT and FRT. Finally, Experiment verifies the practical operability of the proposed strategy.

INDEX TERMS DC-based DFIG, perturbation observer, single-loop controller, MPPT, FRT.

I. INTRODUCTION

Doubly fed induction generator (DFIG) is extensively employed in wind power generation due to its variable speed operation and exceptional power density [1]. In recent years, high-voltage direct current (HVDC) has been adopted by large wind farms for grid connection, especially offshore remote wind farms [2], [3]. Therefore, the exploration of double-voltage-source-converter DFIG (double-VSC DFIG) that can be connected to a DC-grid holds immense practical significance [4], [5], [6]. Its structure is shown in Fig. 1 [7], The stator and rotor of DFIG are connected to DC-grid through the stator-side converter (SSC) and rotor-side converter (RSC), respectively. The SSC provides a stable DC voltage output to the DC-grid, while the RSC achieves maximum power point tracking (MPPT) by adjusting both the rotor-side current and angular frequency.

The associate editor coordinating the review of this manuscript and approving it for publication was Xiaodong Liang.

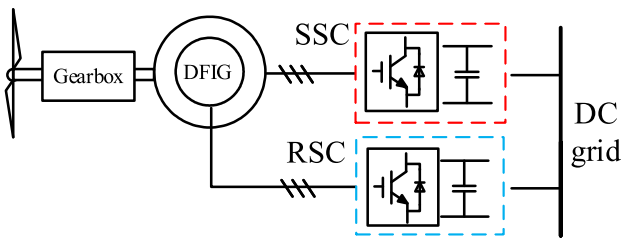

FIGURE 1. Configuration of Double-VSC DFIG.

The modeling and control strategy of AC-based DFIG cannot be directly applied to double-VSC DFIG systems, relevant research on double-VSC DFIG has thus been extensively conducted. The traditional linear control strategy used to realize the stator-rotor coordinated MPPT control, for example, air-gap flux orientation control [7], stator flux orientation control [8], model predictive control [9], single-loop finite control set model predictive control [10], single-loop feedback linearization control [11]. However, the

© 2024 The Authors. This work is licensed under a Creative Commons Attribution-NonCommercial-NoDerivatives 4.0 License.
For more information, see https://creativecommons.org/licenses/by-nc-nd/4.0/

conventional linear control strategy exhibits certain inherent limitations that cannot be disregarded, including reliance on system models, inadequate model accuracy, suboptimal efficiency, and unsatisfactory transient performance [12], [13]. Therefore, nonlinear control strategies are used in this system. The sliding mode control strategy is employed in [14] to enhance the system's robustness. In [15] designed an adaptive controller based on the stator flux observer, aiming to mitigate the reliance on system models.

In any case, the DFIG wind turbine system is inherently characterized by high nonlinearity. In addition to encountering parameter disturbances arising from operational changes in system parameters, as well as transient disturbances caused by external aerodynamics, unmodeled factors, and grid faults [16]. The primary objective of designing a control strategy for DFIG is to effectively harness the maximum wind energy while ensuring compliance with fault-ride-through (FRT) benchmark capability [17]. However, the aforementioned disturbances, which are almost impossible to measure, pose significant challenges in achieving these control objectives.

Currently, the PID controller remains extensively employed in industrial production due to its inherent advantages of simplistic structure and exceptional reliability. The drawback of PID control lies in the fact that its control parameters are determined through single point linearization of the controlled system. Consequently, when disturbances cause changes in the stability of the controlled system, there is a possibility for a decline or even failure in achieving the desired control objective [18]. At this point, one of the solutions is to estimate perturbation from measurable variable and then compensate for it in the control strategy. The most representative perturbation observers are high-gain perturbation observer (HPO) [19] and sliding-mode perturbation observer (SPO) [20]. The operating principle entails characterizing all unknown, time-varying internal and external perturbations as a perturbation term, subsequently subjecting it to observation. However, compared with SPO, the significant change in the transient response of the system can easily induce the peak phenomenon of HPO [21]. Additionally, the convergence rate of observation error for SPO is faster than that of HPO [22], and even fixed-time perturbation observation can be achieved, which is not affected by the initial state of the system [23]. The implementation of SPO in AC-based DFIG system leads to the following achievements. In [24], a state feedback controller based on sliding-mode state and perturbation observer (SMSPO) for AC-based DFIG is introduced, where the stator reactive power of voltage vector-oriented decoupling is utilized as the system state variable. Based on the aforementioned paper, the multi-objective grasshopper optimization algorithm is added in [25] to enhance the dynamic performance of the system. A 6-order AC-based DFIG model is utilized by [26] to decouple four subsystems, and four SMSPOs are designed to observe the state and perturbation term. This approach results in excellent anti-disturbance control performance, including interference generated by external power systems. The utilization SMSPO based damping control is proposed in [27] for AC-based DFIG, with the aim of mitigating inter-area oscillations in multi-area power systems.

TABLE 1. Nomenclatures.

$u_{rd}, u_{rq}, u_{sd}, u_{sq}$	rotor and stator voltages in d/q frame
ψ_{sd}, ψ_{sq}	stator flux in d/q frame
i_{rd}, i_{rq}	rotor currents in d/q frame
$\omega_1, \omega_r, \omega_s$	synchronous rotating and rotor angular speed, $\omega_s = \omega_1 - \omega_r$
R_s, R_r	stator and rotor winding resistances
L_m, L_r, L_s	mutual inductance, stator and rotor inductance
T_e, T_m	electromagnetic torque, mechanical torque
J, n_p	inertial moment and pole pairs of the motor
V_{wind}, R_{wt}	wind speed, radius of wind turbine
C_{pmax}	the maximum power coefficient of wind energy captured by the wind turbine
$\lambda, \beta, \lambda_{opt}$	tip speed ratio, pitch angle and optimal tip speed ratio of wind turbine

This paper proposes a robust decoupling controller based on perturbation observer (RDC-PO) for double-VSC DFIG, aiming to achieve integrated control. The summarization of the paper's innovation and contribution can be outlined as follows:

1) In this paper, the intermediate link of the traditional cascaded double-loop structure is eliminated, and a single-loop decoupling structure is adopted. This approach not only improves the sensitivity of the system reaction, but also reduces the number of control parameters.
2) The proposed controller is capable of online estimation and compensation for all unknown, time-varying internal and external perturbations, including perturbations arising from power system faults.
3) In contrast to feedback linearization controller [11], the proposed controller does not require a precise system model and is more straightforward to put into practice.
4) The simulation results in three distinct cases demonstrate the improved performance of the proposed controller compared with double-loop feedback controller (DFC) and single-loop feedback control (SFC).

The remaining sections of the paper are structured in the following manner. The double-VSC DFIG system model is built in Section II. The proposed RDC-PO strategies are designed in Section III. The simulations are in Section IV. The experiments are in Section V. The conclusions are made in Section VI.

II. SYSTEM MODELLING

A. WIND TURBINE

The turbine power characteristics curve of the wind turbine is depicted in the Fig. 2 [11], the red line represents the maximum mechanical energy captured by the wind turbine at $\lambda = \lambda_{opt}$, this moment, the turbine speed is

$$\omega_m = \frac{\lambda_{opt} V_{wind}}{R_{wt}} \tag{1}$$

This paper assumes that the turbine speed is equal to rotor speed. So, the DFIG rotor angular speed reference is

$$\omega_r^* = \frac{\lambda_{opt} V_{wind}}{R_{wt}} \approx 0.1 V_{wind} \tag{2}$$

B. DOUBLE-VSC DFIG

The dynamics of a dual-VSC DFIG can be characterized as [11]

$$\begin{cases} \dfrac{d\psi_{sd}}{dt} = -\dfrac{R_s}{L_s}\psi_{sd} + \omega_1\psi_{sq} + C_b R_s i_{rd} + u_{sd} \\ \dfrac{d\psi_{sq}}{dt} = -\omega_1\psi_{sd} - \dfrac{R_s}{L_s}\psi_{sq} + C_b R_s i_{rq} + u_{sq} \\ \dfrac{di_{rd}}{dt} = \dfrac{C_b R_s}{C_a L_s}\psi_{sd} - \dfrac{C_b}{C_a}\omega_r\psi_{sq} - \dfrac{R_r + C_b^2 R_s}{C_a} i_{rd} \\ \qquad +(\omega_1 - \omega_r) i_{rq} - \dfrac{C_b}{C_a} u_{sd} + \dfrac{1}{C_a} u_{rd} \\ \dfrac{di_{rq}}{dt} = \dfrac{C_b}{C_a}\omega_r\psi_{sd} + \dfrac{C_b R_s}{C_a L_s}\psi_{sq} \\ \qquad -\omega_s i_{rd} - \dfrac{R_r + C_b^2 R_s}{C_a} i_{rq} - \dfrac{C_b}{C_a} u_{sq} + \dfrac{1}{C_a} u_{rq} \\ \dfrac{d\omega_r}{dt} = \dfrac{3n_p^2 L_m}{2JL_s}(\psi_{sd} i_{rq} - \psi_{sq} i_{rd}) - \dfrac{n_p}{J} T_m \end{cases} \tag{3}$$

where $C_a = (L_r L_s - L_m^2)/L_s$, $C_b = L_m/L_s$.

III. RDC-PO CONTROL STRATEGY

Equation (3) reveals that dual-VSC DFIG is a multi-input multi-output complex coupled system. According to the system configuration (Fig. 1), it has four control inputs (u_{sd}, u_{sq}, u_{rd}, u_{rq}). Based on the control objective of efficient utilization of maximum wind energy, the state variables and control inputs are both determined as $[\psi_{sd}\ \psi_{sq}\ \omega_r\ i_{rq}]$. On the basis of retaining all the dynamic characteristics of the system, the first derivative of ω_r in (3) is further derived. The system state matrix is arranged as

$$\begin{bmatrix} \dot{\psi}_{sd} \\ \dot{\psi}_{sq} \\ \ddot{\omega}_r \\ \dot{i}_{rq} \end{bmatrix} = \begin{bmatrix} f_1 \\ f_2 \\ f_3 \\ f_4 \end{bmatrix} + B \begin{bmatrix} u_{sd} \\ u_{sq} \\ u_{rd} \\ u_{rq} \end{bmatrix}$$

$$f_1 = -\frac{R_s}{L_s}\psi_{sd} + \omega_1\psi_{sq} + C_b R_s i_{rd}$$

$$f_2 = -\omega_1\psi_{sd} - \frac{R_s}{L_s}\psi_{sq} + C_b R_s i_{rq}$$

$$\begin{aligned} f_3 = C_c[&(-\frac{R_s}{L_s} - \frac{R_r + C_b^2 R_s}{C_a})\psi_{sd} i_{rq} \\ &+ \omega_r(\psi_{sq} i_{rq} + \psi_{sd} i_{rd}) \\ &+ (\frac{R_s}{L_s} + \frac{R_r + C_b^2 R_s}{C_a})\psi_{sq} i_{rd} \\ &+ \frac{C_b}{C_a}\omega_r(\psi_{sd}^2 + \psi_{sq}^2)] - \frac{n_p}{J}\dot{T}_m \end{aligned}$$

$$f_4 = \frac{C_b}{C_a}\psi_{sd}\omega_r + \frac{C_b R_s}{C_a L_s}\psi_{sq} - \omega_s i_{rd} - \frac{R_r + C_b^2 R_s}{C_a} i_{rq}$$

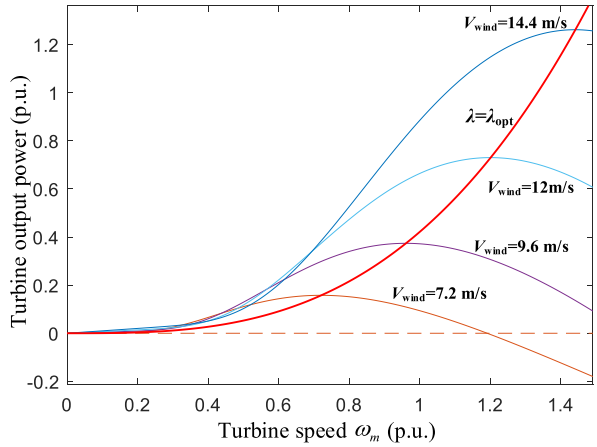

FIGURE 2. Turbine power characteristics ($\beta = 0$).

$$B = \begin{bmatrix} 1 & 0 & 0 & 0 \\ 0 & 1 & 0 & 0 \\ C_c(i_{rq} + \frac{C_b}{C_a}\psi_{sq}) & -C_c(i_{rd} + \frac{C_b}{C_a}\psi_{sd}) & \frac{-C_c}{C_a}\psi_{sq} & \frac{C_c}{C_a}\psi_{sd} \\ 0 & -\frac{C_b}{C_a} & 0 & \frac{1}{C_a} \end{bmatrix} \tag{4}$$

where $C_c = (3n_p^2 L_m)/(2JL_s)$. $\dot{T}_m$ is calculated by Backward Difference Euler Formula (5). B is the control gain matrix, det(B)= $-\frac{C_c}{C_a^2}\psi_{sq}$ and by (21) known $\psi_{sq} \neq 0$, so B is invertible. Although the system is decoupled, matrix B is too complex.

$$\frac{dT_m}{dt} = \frac{\Delta T_m(k)}{\Delta t} \approx \frac{T_m(k) - T_m(k-1)}{\Delta t} \tag{5}$$

where $T_m(k)$ and $T_m(k-1)$ are obtained by measurement, even if there is a measurement error to create system perturbation, it will be compensated by the controller behind.

A. DEFINE THE PERTURBATION TERM

Assuming that all system perturbations are unknown, define the perturbation terms $\Psi_i(\cdot)$ ($i = 1, 2, 3, 4$) for system (4) as

$$\begin{bmatrix} \Psi_1(\cdot) \\ \Psi_2(\cdot) \\ \Psi_3(\cdot) \\ \Psi_4(\cdot) \end{bmatrix} = \begin{bmatrix} f_1 \\ f_2 \\ f_3 \\ f_4 \end{bmatrix} + (B - B_0) \begin{bmatrix} u_{sd} \\ u_{sq} \\ u_{rd} \\ u_{rq} \end{bmatrix} \tag{6}$$

where B_0 is a constant matrix,

$$B_0 = \begin{bmatrix} b_{01} & 0 & 0 & 0 \\ 0 & b_{02} & 0 & 0 \\ 0 & 0 & b_{03} & 0 \\ 0 & 0 & 0 & b_{04} \end{bmatrix}$$

Physical limitations impose local bounds on control inputs and state variables, so $\Psi_i(\cdot)$ and derivative $\dot{\Psi}_i(\cdot)$ are bounded, and $\Psi_i(0, 0, 0) = 0$, $\dot{\Psi}_i(0, 0, 0) = 0$. From (4) to know, in the matrix B, $b_{11} = 1$, $b_{22} = 1$, $b_{33} = \frac{-C_c}{C_a}\psi_{sq} > 0$, and $b_{44} = \frac{1}{C_a} > 0$, so b_{0i} ($i = 1, 2, 3, 4$) are chosen to fulfill $b_{01} > \frac{1}{2}$, $b_{02} > \frac{1}{2}$, $b_{03} > \frac{-C_c}{2C_a}\psi_{sq}$, and $b_{04} > \frac{1}{2C_a}$.

Put (6) into (4),

$$\begin{bmatrix} \dot{\psi}_{sd} \\ \dot{\psi}_{sq} \\ \dot{\omega}_r \\ \dot{i}_{rq} \end{bmatrix} = \begin{bmatrix} \Psi_1(\cdot) \\ \Psi_2(\cdot) \\ \Psi_3(\cdot) \\ \Psi_4(\cdot) \end{bmatrix} + B_0 \begin{bmatrix} u_{sd} \\ u_{sq} \\ u_{rd} \\ u_{rq} \end{bmatrix} \tag{7}$$

Define $z_{11} = \psi_{sd}$, $z_{12} = \Psi_1(\cdot)$, $z_{21} = \psi_{sq}$, $z_{22} = \Psi_2(\cdot)$, $z_{31} = \omega_r$, $z_{32} = \dot{\omega}_r$, $z_{33} = \Psi_3(\cdot)$, $z_{41} = i_{rq}$, and $z_{42} = \Psi_4(\cdot)$. Hence, the system (7) can be represented by four subsystems, are

$$\begin{cases} \dot{z}_{11} = z_{12} + b_{01}u_{sd} \\ \dot{z}_{12} = \dot{\Psi}_1(\cdot) \\ y_1 = z_{11} = \psi_{sd} \end{cases} \quad \begin{cases} \dot{z}_{21} = z_{22} + b_{02}u_{sq} \\ \dot{z}_{22} = \dot{\Psi}_2(\cdot) \\ y_2 = z_{21} = \psi_{sq} \end{cases}$$

$$\begin{cases} \dot{z}_{31} = z_{32} \\ \dot{z}_{32} = z_{33} + b_{03}u_{rd} \\ \dot{z}_{33} = \dot{\Psi}_3(\cdot) \\ y_3 = z_{31} = \omega_r \end{cases} \quad \begin{cases} \dot{z}_{41} = z_{42} + b_{04}u_{rq} \\ \dot{z}_{42} = \dot{\Psi}_4(\cdot) \\ y_4 = z_{41} = i_{rq} \end{cases} \tag{8}$$

B. DESIGN OF SPO

The state observer is then designed to estimate the states of the four subsystems within system (8). It should be noted that the design of the four subsystems in system (9) follows a similar structure, To enhance readability, the design process of the proposed controller is exemplified using the third order ω_r-subsystem. The control design procedure for the remaining three second-order subsystems follows the same method. The estimation of the ω_r-subsystem is provided as follows.

$$\begin{cases} \dot{\hat{z}}_{31} = \hat{z}_{32} + \beta_{31}\bar{z}_{31} + k_{31}\tanh(\frac{\bar{z}_{31}}{\varepsilon}) \\ \dot{\hat{z}}_{32} = \hat{\Psi}_3(\cdot) + \beta_{32}\bar{z}_{31} + k_{32}\tanh(\frac{\bar{z}_{31}}{\varepsilon}) + b_{03}u_{rd} \\ \dot{\hat{\Psi}}_3(\cdot) = \beta_{33}\bar{z}_{31} + k_{33}\tanh(\frac{\bar{z}_{31}}{\varepsilon}) \end{cases} \tag{9}$$

where gains β_{3i} and k_{3i} (i=1, 2, 3) are positive constants. the symbol '^' and '¯' denotesan estimate and error of states. The continuous smooth function $\tanh(\frac{\bar{z}_{31}}{\varepsilon})$ is adopted to reduce the chattering, it is defined as

$$\tanh(\frac{\bar{z}_{31}}{\varepsilon}) = \frac{e^{\frac{\bar{z}_{31}}{\varepsilon}} - e^{-\frac{\bar{z}_{31}}{\varepsilon}}}{e^{\frac{\bar{z}_{31}}{\varepsilon}} + e^{-\frac{\bar{z}_{31}}{\varepsilon}}}$$

The layer thickness constant $\varepsilon > 0$ expected close to 0. Chattering can be effectively reduced by substituting the symbolic function $sgn(x)$ with a continuous smooth function $\tanh(\frac{x}{\varepsilon})$.

The state estimation error $\bar{z}_{3i} = z_{3i} - \hat{z}_{3i}$, $(i = 1, 2, 3)$ is given form (8) and (9),

$$\begin{cases} \dot{\bar{z}}_{31} = \bar{z}_{32} - \beta_{31}\bar{z}_{31} - k_{31}\tanh(\frac{\bar{z}_{31}}{\varepsilon}) \\ \dot{\bar{z}}_{32} = \bar{z}_{33} - \beta_{32}\bar{z}_{31} - k_{32}\tanh(\frac{\bar{z}_{31}}{\varepsilon}) \\ \dot{\bar{z}}_{33} = \dot{\Psi}_3(\cdot) - \beta_{33}\bar{z}_{31} - k_{33}\tanh(\frac{\bar{z}_{31}}{\varepsilon}) \end{cases} \tag{10}$$

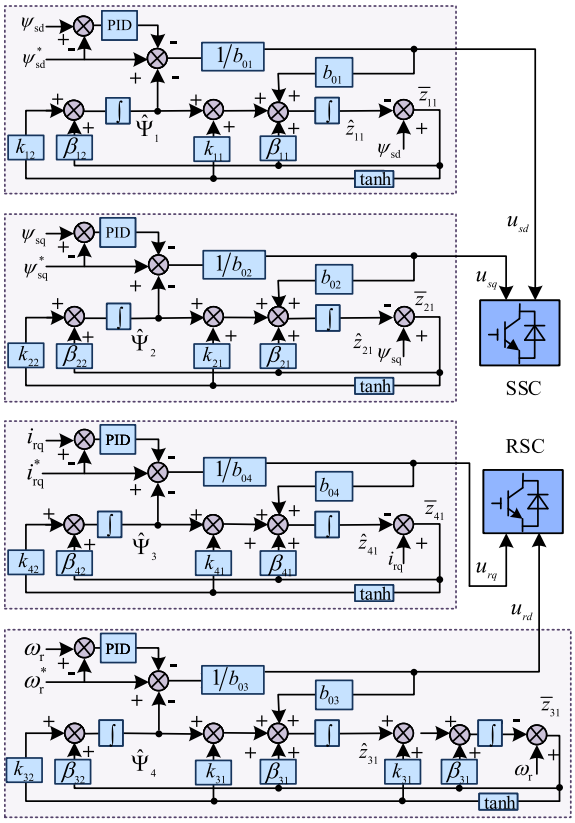

FIGURE 3. The RDC-PO of double-VSI DFIG.

The defined sliding surface $S(\bar{z}) = \bar{z}_{31} = 0$ pertains to the observer. Define the Lyapunov function $V = \frac{1}{2}S^2$, whose derivative is

$$\begin{aligned} \dot{V} &= \bar{z}_{31}\dot{\bar{z}}_{31} = \bar{z}_{31}(\bar{z}_{32} - \beta_{31}\bar{z}_{31} - k_{31}\tanh(\frac{\bar{z}_{31}}{\varepsilon})) \\ &\le (|\bar{z}_{32}| - k_{31})\,|\bar{z}_{31}| - \beta_{31}\bar{z}_{31}^2 + k_{31}\varepsilon \end{aligned} \tag{11}$$

As long as $k_{31} \ge |\bar{z}_{32}|_{max}$, then

$$\dot{V} \le -\beta_{31}\bar{z}_{31}^2 + k_{31}\varepsilon \le -2\beta_{31}V + k_{31}\varepsilon \tag{12}$$

Thus, can be obtained

$$V \le \frac{k_{31}\varepsilon}{2\beta_{31}}, \quad as\ t \to \infty \tag{13}$$

namely,

$$|\bar{z}_{31}| \le \sqrt{\frac{k_{31}\varepsilon}{2\beta_{31}}}, \quad as\ t \to \infty \tag{14}$$

It can be seen from (14) that $\tanh(\frac{x}{\varepsilon})$ brings the following result after replacing $sgn(x)$.

1) The presence of ε causes the error of SPO to converge not to 0 in finite time, but to a neighborhood around zero.
2) Even if ε can be arbitrarily small and β_{31} arbitrarily large (regardless of noise), a steady-state error still persists in the SPO. In fact, if $\varepsilon = 0$, $\tanh(\frac{\bar{z}_{31}}{\varepsilon}) = sgn(\bar{z}_{31})$, then $\dot{V} \le (|\bar{z}_{32}| - k_{31})\,|\bar{z}_{31}| - \beta_{31}\bar{z}_{31}^2$, select

TABLE 2. Parameters of DFIG.

Parameters	Quantity
Maximum stator power	3.0 kw
Stator voltage	311 V 50 Hz
Pole pairs	2
Stator resistance	0.88 Ω (0.014 p.u.)
Rotor resistance	0.88 Ω (0.014 p.u.)
Stator leakage inductance	5.6 mH (0.028 p.u.)
Rotor leakage inductance	5.6 mH (0.028 p.u.)
Mutual inductance	87.5 mH (0.442 p.u.)
Inertia constant	0.015 $kg.m^2$ (0.079 s)
Synchronous speed	1500 r/min
Rated rotor speed	1680 rpm
DC voltage	650 V

$k_{31} \geq |\bar{z}_{32}|_{max}$, it is obvious that $\bar{z}_{31} \to 0$ as $t \to t_s$ and $\bar{z}_{31} = 0$ for $t > t_s$.

Anyway, the convergence of the observer's error $\bar{z}_{31}$ is guaranteed by selecting $k_{31} \geq |\bar{z}_{32}|_{max}$.

According to [28], The form of the error dynamics on the sliding mode is given by

$$\begin{cases} \dot{\bar{z}}_{32} = -\dfrac{k_{32}}{k_{31}}\bar{z}_{32} + \bar{z}_{33} \\ \dot{\bar{z}}_{33} = -\dfrac{k_{33}}{k_{31}}\bar{z}_{32} + \dot{\Psi}_3(\cdot) \end{cases} \tag{15}$$

The selection of $\frac{k_{3i}}{k_{31}}$ (i=2, 3) follows the Luenberger observer method, so, the root of $p^2 + \frac{k_{32}}{k_{31}}p + \frac{k_{33}}{k_{31}} = (p + \lambda_{k3})^2 = 0$ is in the open left-half complex plane. And, the β_{3i} are chosen to be the Luenberger observer (which would match with $k_{3i} = 0$ (i=1, 2, 3)), therefore, the root of $s^3+\beta_{31}s^2+\beta_{32}s+\beta_{33} = (s+\lambda_{s3})^3 = 0$ is in the open left-half complex plane. Thus, β_{3i} and k_{3i} satisfy the above conditions, the perturbation observer will converge to a vicinity of the origin, as demonstrated in [28], [29], and [30].

C. DESIGN OF RDC-PO

According to the requirement of the MPPT, the output tracking error $e = [e_1\ e_2\ e_3\ e_4]^T$ is defined as $e_1 = \psi_{sd} - \psi_{sd}^*$, $e_2 = \psi_{sq} - \psi_{sq}^*$, $e_3 = \omega_r - \omega_r^*$, $e_4 = i_{rq} - i_{rq}^*$, where ψ_{sd}^*, ψ_{sq}^*, ω_r^*, and i_{rq}^* are the tracking values of the system.

Based on the system (7) and the perturbation observer (9), the controller is designed as,

$$\begin{bmatrix} u_{sd} \\ u_{sq} \\ u_{rd} \\ u_{rq} \end{bmatrix} = B_0^{-1} \begin{bmatrix} \dot{\psi}_{sd}^* - \hat{\Psi}_1(\cdot) - k_{p1}e_1 - k_{i1}\int e_1 dt - k_{d1}\frac{de_1}{dt} \\ \dot{\psi}_{sq}^* - \hat{\Psi}_2(\cdot) - k_{p2}e_2 - k_{i2}\int e_2 dt - k_{d2}\frac{de_2}{dt} \\ \ddot{\omega}_r^* - \hat{\Psi}_3(\cdot) - k_{p3}e_3 - k_{i3}\int e_3 dt - k_{d3}\frac{de_3}{dt} \\ \dot{i}_{rq}^* - \hat{\Psi}_4(\cdot) - k_{p4}e_4 - k_{i4}\int e_4 dt - k_{d4}\frac{de_4}{dt} \end{bmatrix} \tag{16}$$

Parameters $k_{pi}, k_{ii}, k_{di}, (i = 1, 2..4)$ are positive and satisfy $k_{di}\ddot{e}_i + k_{pi}\dot{e}_i + k_{ii}e_i = 0$ to ensure the stability of tracking error dynamics. The block diagram of RDC-PO is shown in Fig. 3.

Then the ω_r-subsystem is taken as an example to prove the stability of the controller (16).

According to $e_3 = \omega_r - \omega_r^*$, that

$$\ddot{e}_3 = \ddot{\omega}_r - \ddot{\omega}_r^* \tag{17}$$

Put (7) into (17),

$$\ddot{e}_3 = \Psi_3(\cdot) + b_{03}u_{rd} - \ddot{\omega}_r^* \tag{18}$$

TABLE 3. Parameters of controllers.

1.The PID parameters of RDC-PO (16)
$k_{p1} = 100$; $k_{i1} = 20$; $k_{d1} = 0$; $k_{p2} = 100$; $k_{i2} = 20$; $k_{d2} = 0$;
$k_{p3} = 2000$; $k_{i3} = 100$; $k_{d3} = 100$; $k_{p4} = 200$; $k_{i4} = 20$; $k_{d4} = 0$.
2.SPO parameters (9)
$\varepsilon = 0.02$
$\lambda_{sj} = -20$; $\beta_{j1} = 40$; $\beta_{j2} = 400$;
$\lambda_{kj} = -40$; $k_{j1} = 75$; $k_{j2} = 37500$; $j = 1, 2, 4$
$\lambda_{s3} = -10$; $\beta_{31} = 30$; $\beta_{32} = 300$; $\beta_{33} = 1000$
$\lambda_{k3} = -10$; $k_{31} = 20$; $k_{32} = 600$; $k_{33} = 6000$.
3.The PI parameters of SFC
$k'_{p1} = 500$; $k'_{i1} = 200$; $k'_{p2} = 550$; $k'_{i2} = 220$;
$k'_{p3} = 8000$; $k'_{i3} = 5000$;
(At random wind speed: $k'_{p3} = 4000$; $k'_{i3} = 2000$;$k'_{d3} = 200$)
$k'_{p4} = 100$; $k'_{i4} = 150$.
4.The PI parameters of DFC
SSC:$k'_{pd} = 600$; $k'_{id} = 400$; $k'_{pq} = 650$; $k'_{iq} = 420$;
RSC: $k'_{p\omega} = 2000$; $k'_{i\omega} = 1500$; $k'_{pid} = 50$; $k'_{iid} = 20$.
$k'_{pQ} = 1000$; $k'_{iQ} = 800$; $k'_{piq} = 50$; $k'_{iiq} = 12$.

Let $u_{rd} = \frac{1}{b_{03}}(\ddot{\omega}_r^* - \hat{\Psi}_3(\cdot) + u_1)$, where $u_1 = -k_{p3}e_3 - k_{i3}\int e_3 dt - k_{d3}\frac{de_3}{dt}$, and $\hat{\Psi}_3(\cdot)$ is provided by sliding-mode perturbation observer (9). If the gains β_{3i} and $k_{3i}(i = 1, 2, 3)$ are chosen properly, exist for a certain time T, when $t \geq T$, $\hat{\Psi}_3(\cdot) \equiv \Psi_3(\cdot)$, at this time $\ddot{e}_3 = u_1$.

Define $z_a = e_3$, $z_b = \dot{e}_3$, $z_c = \ddot{e}_3$, then

$$\begin{cases} \dot{z}_a = z_b \\ \dot{z}_b = z_c \\ \dot{z}_c = \dddot{e}_3 = \dot{u}_1 = -k_{p3}z_b - k_{i3}z_a - k_{d3}z_c \end{cases} \tag{19}$$

Define $z = [z_a\ z_b\ z_c]^T$, then (19) can be expressed as

$$\dot{z} = Az = \begin{bmatrix} 0 & 1 & 0 \\ 0 & 0 & 1 \\ -k_{i3} & -k_{p3} & -k_{d3} \end{bmatrix} z \tag{20}$$

where, select $k_{pi}, k_{ii}, k_{di}, (i = 1, 2..4)$ are positive and satisfy $k_{di}\ddot{e}_i + k_{pi}\dot{e}_i + k_{ii}e_i = 0$, namely, A is a Hurwitz matrix, $\lim_{t\to\infty} z_a(t) = 0$.

The rotor speed reference ω_r^* is shown in (2), other reference values are determined as follows. A stator-oriented flux frame is adopted with its vector direction aligned with the $q - axis$, the stator flux reference value (ψ_s^*) and its d-q components are given

$$\begin{cases} \psi_{sd}^* = 0 \\ \psi_{sq}^* = \psi_s^* = -\dfrac{V_s}{\omega_1} \end{cases} \tag{21}$$

where V_s is generator rated voltage amplitude. According to (3) and (21), the rotor current reference value is obtained:

$$i_{rq}^* = -\frac{\psi_s^*}{L_m} \tag{22}$$

It is should be noted that the controller adopt B_0, which completely decouples the system (4) into four simple single-output single-input systems. Moreover, the implementation of the proposed controllers only need the measured rotor speed and stator-rotor currents.

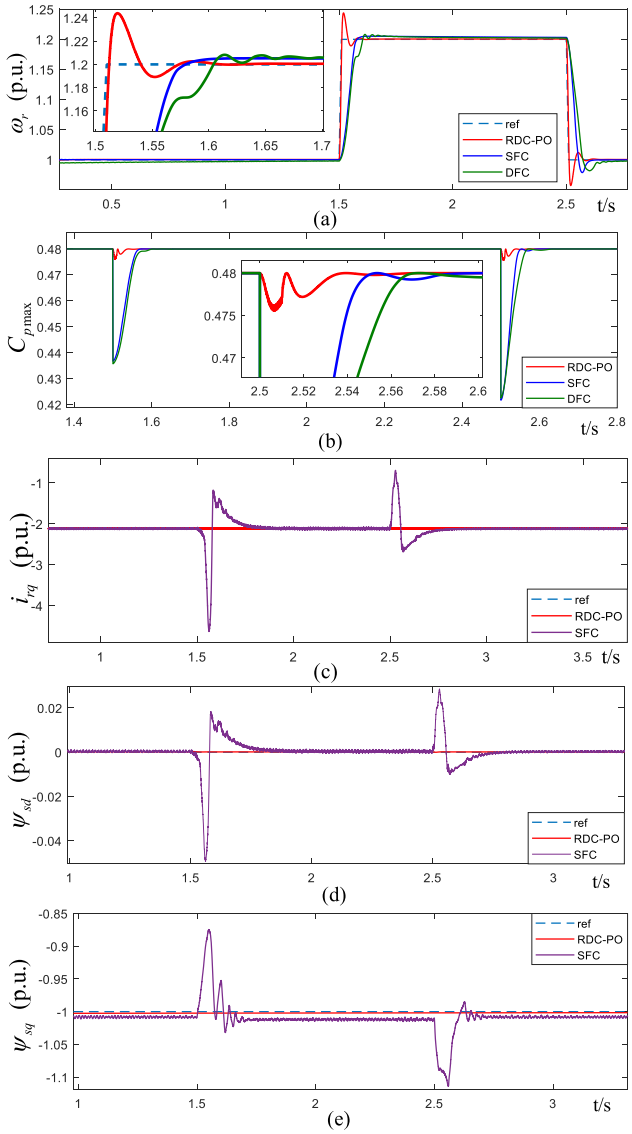

FIGURE 4. System transient performance.
(DFC: double- loop feedback controller; SFC: single-loop feedback controller; RDC-PO: the proposed controller).

Considering the tolerance range of SSC and RSC, u_{sd}, u_{sq}, u_{rd}, and u_{rq} are scaled proportionally as [31]: $u_{sd_lim} = u_{sd}v_{max}/u_s$, $u_{sq_lim} = u_{sq}v_{max}/u_s$, $u_{rd_lim} = u_{rd}v_{max}/u_s$, and $u_{rq_lim} = u_{rq}v_{max}/u_s$, where $u_s = \sqrt{u_{sd}^2 + u_{sq}^2}$, $u_r = \sqrt{u_{rd}^2 + u_{rq}^2}$. With SPWM modulation strategy, the maximum amplitude of the phase voltage is $V_{dc}/2$, so $v_{max} = V_{dc}/2$.

IV. SIMULATION RESULTS

In order to comprehensively demonstrate the performance of the proposed controller, four simulation scenarios have been devised for comparative analysis against benchmarks double-loop feedback controller (DFC) and single-loop feedback controller (SFC) [11]. The system parameters are given in Table 2 and physical units of the simulated system are p.u.. SPO and RDC-PO parameters as shown in the Table 3.

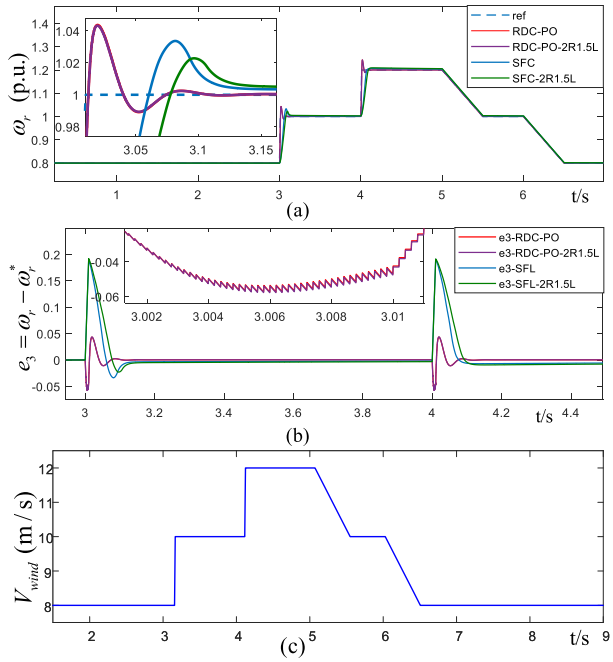

FIGURE 5. Robustness of system parameter uncertainty.
(SFC: single-loop feedback controller; RDC-PO: the proposed controller).

A. TRANSIENT PERFORMANCE

A stepped wind is designed to rapidly rise and fall between 10m/s and 12m/s at 1.5s and 2.5s to observe the transient performance of the proposed controller. Fig. 4(a) shows the tracking results of the system rotor angular frequency ω_r under three controllers. Although there is an overshoot of 3.3%, it is within a reasonable range. The superior transient performance of RDC-PO is further highlighted in Fig. 4(b), which demonstrates whether the system can run under MPPT. As depicted in the figure, RDC-PO exhibits a remarkable increase in output power, up to 12 times higher compared to the other two controllers. The other outputs of the system are shown in the Fig. 4(c)-(e), and RDC-PO achieves almost complete decoupling.

B. ROBUSTNESS OF SYSTEM PARAMETER UNCERTAINTY

The design wind speed is illustrated in the Fig. 5(c) to assess the system's robustness against uncertain parameters and external disturbances caused by wind. Assuming a 100% mismatch in system resistances ($2R_s$ $2R_r$) and a 50% mismatch in mutual inductance ($1.5L_m$) around the nominal value.

The rotor angular frequencys ω_r tracking of the two controllers under different system parameters are shown in the Fig. 5(a). Tracking errors $e_3 = \omega_r - \omega_r^*$ shown in the Fig. 5(b). The impact of parameter perturbation on RDC-PO is found to be negligible, as evidenced by the results depicted in these two figures.

C. ROBUSTNESS UNDER RANDOM WIND DISTURBANCE

A random wind speed perturbation model is shown in the Fig. 6(a) to observe the performance and controllability of

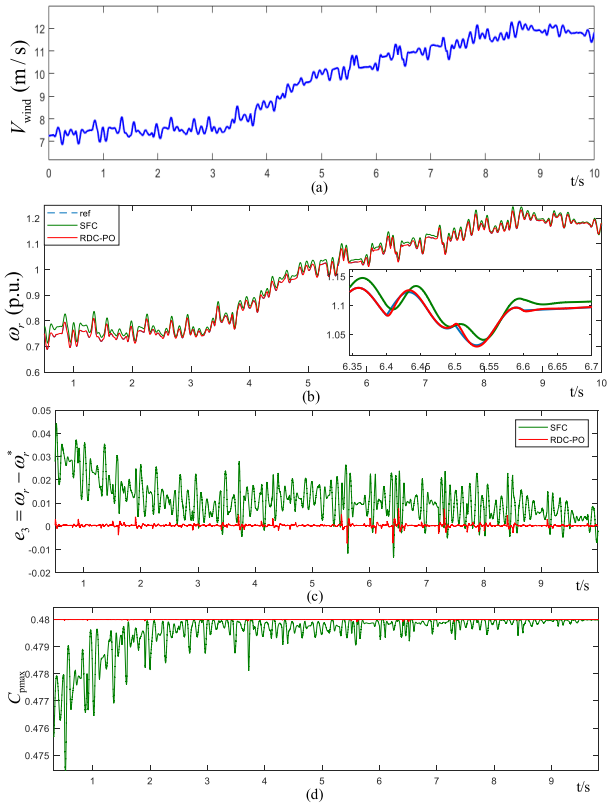

FIGURE 6. Robustness under random wind disturbance.
(SFC: single-loop feedback controller; RDC-PO: the proposed controller).

the controllers. Due to the frequent fluctuation of random wind, the reference value ω_r^* oscillates. In this case, the SFC controller needs to add differential terms to suppress oscillations, and its ω_r-subsystem controller parameters are revised as follows: $k'_{p3} = 4000$, $k'_{i3} = 2000$, $k'_{d3} = 200$.

Based on the simulation results depicted in Fig. 6(b)-(d), the RDC-PO exhibits remarkable effectiveness in showcasing both its ability to dampen oscillations and control rotor angular frequency. Additionally, the power coefficient closely approximates the optimal value, signifying successful achievement of maximum wind energy under perturbed conditions. On the contrary, SFC adds a differential term, which still oscillates violently compared to RDC-PO.

D. FRT CAPABILITY

The stator side of Double-VSC DFIG is connected to the power grid through a SSC, which enhances its FRT capability compared to that of AC-based DFIG. However, there is still the risk of offline when the power grid fails seriously.

A DC-grid failure is designed, where the voltage decreases from its nominal value to 30% within a time interval of 2.5 s to 2.6 s. The stator active power and rotor current response to the voltage dip were analyzed to evaluate the FRT capability of a double-VSC DFIG with two controllers. Currently, the DFIG is operating steadily at 1.1 p.u. ω_r.

When the stator voltage experiences a significant drop, the rotor side compensates by increasing the currentbalance this

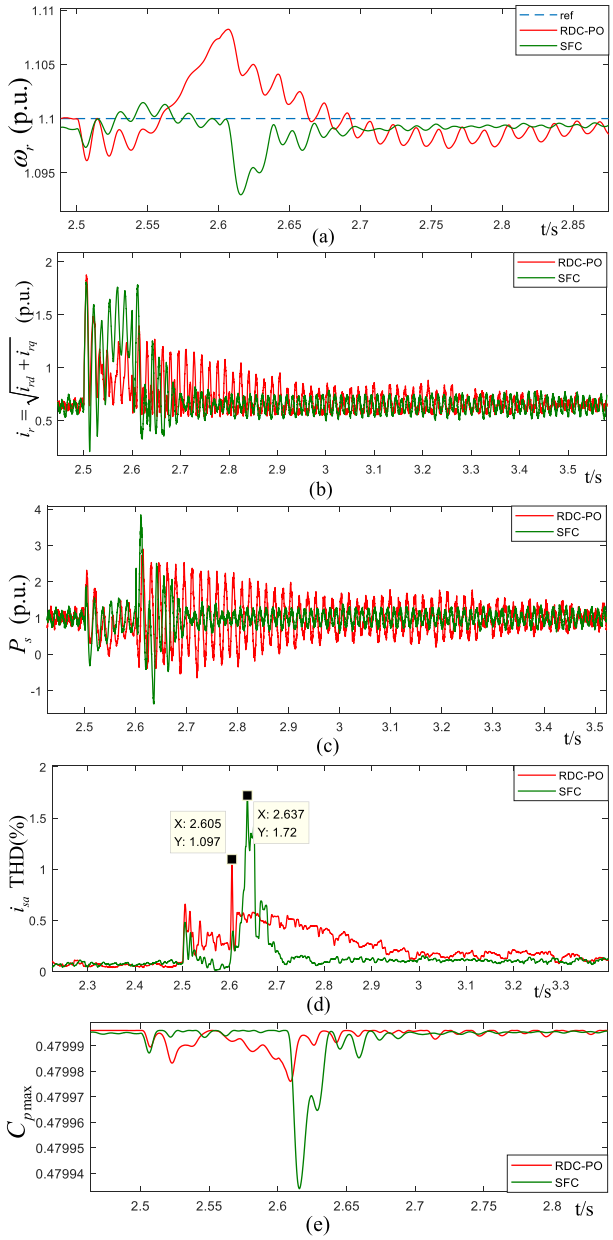

FIGURE 7. FRT capabilities of system.
(SFC: single-loop feedback controller; RDC-PO: the proposed controller).

decrease. However, if a substantial impulse current occurs during this period, it may potentially inflict damage on power electronics and impede wind energy systems [32]. Consequently, the controller will adjust the rotor speed to compensate for the disturbance caused by the drop in stator voltage and thereby regulate the rotor current. As depicted in Fig. 7, RDC-PO suppress system oscillation by augmenting the rotor angular frequency, thereby diminishing the rotor current. However, due to the inherent shortcoming of the sliding-mode, chattering occurs in the recovery process.

V. EXPERIMENTAL VALIDATION

To further validate the effectiveness of RDC-PO, an experimental platform for the double-VSC DFIG system is

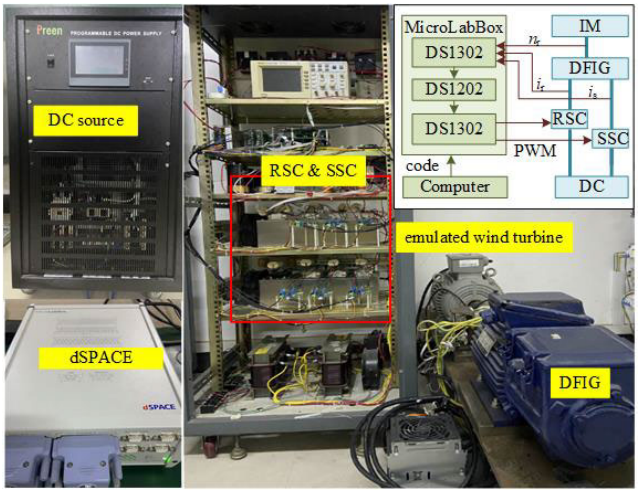

FIGURE 8. System experimental platform.

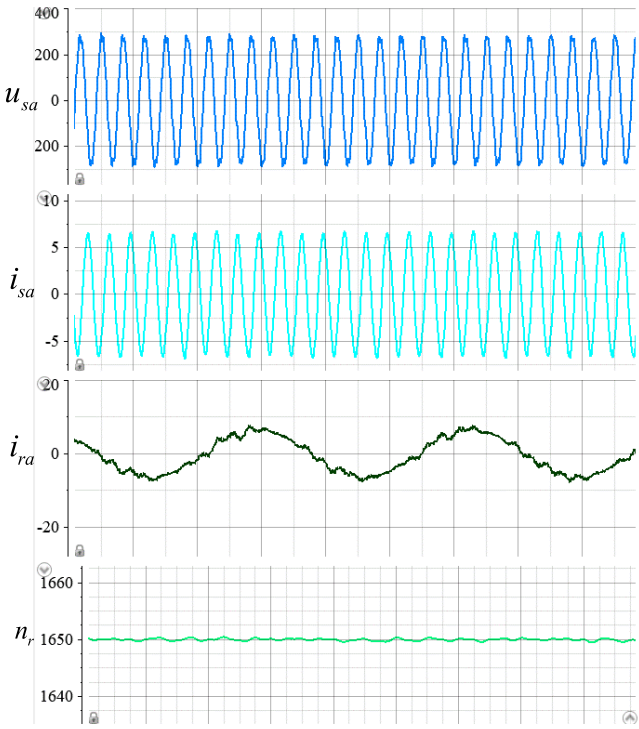

FIGURE 9. Experimental results at wind speed of 11 m/s.

constructed as depicted in Fig. 8, comprising components such as DFIG, RSC, SSC, emulated wind turbine and DC source. The experimental parameters of this system are presented in Table 2. The proposed controllers are implemented on a dSPACE MicroLabBox platform, operating at a sampling frequency of 10 kHz.

A. EXPERIMENTAL RESULTS AT WIND SPEED OF 11 M/S

The experimental design aims to assess the operational stability of the system. The rotor speed n_r of DFIG remains stable at 1650rpm, as shown in the Fig.9, while maintaining a steady sinusoidal waveform for both stator voltage u_{sa}, stator current i_{sa} and rotor current i_{ra} of DFIG.

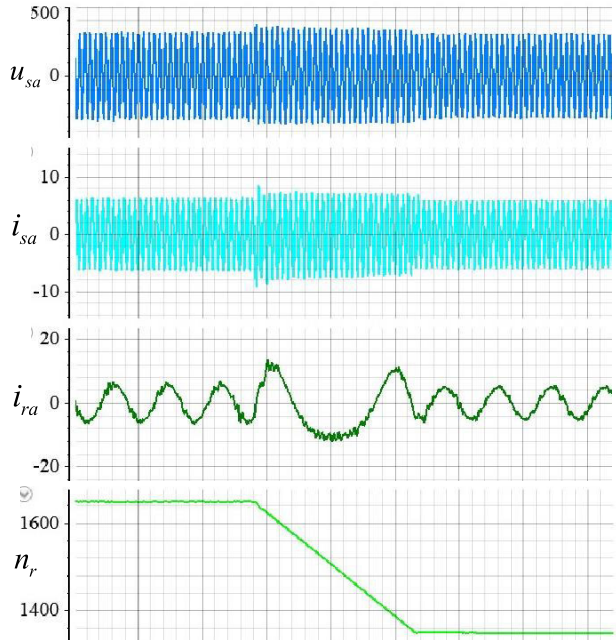

FIGURE 10. Experimental results at variable wind speed.

B. EXPERIMENTAL RESULTS AT VARIABLE WIND SPEED

Design an experiment in which the wind speed gradually drops from 11 m/s to 9 m/s. The rotor speed n_r of DFIG was steadily decreased from 1650 to 1350 rpm, as shown in the Fig.10, the voltage and current (u_{sa}, i_{sa}, i_{ra}) fluctuate within the allowable range.

VI. CONCLUSION

A novel single-loop robust decoupling control method based on perturbation observer (RDC-PO) is proposed for MPPT control of double-VSC DFIG, which can estimate and compensate for all unknown, time-varying internal and external perturbations, including those caused by power system faults. Simulation results demonstrate that the proposed RDC-PO exhibits a rapid dynamic response, robustness to parameter uncertainties, and improved FRT capability. Experimental results validate the practicality and promptness of the control strategy. The sliding-mode perturbation observer possesses the ability to swiftly estimate time-varying perturbations, thereby compensating for the limited range of PID control. In summary, the proposed RDC-PO does not necessitate detailed system model information and when combined with a single-loop PID control strategy, simplifies the controller structure while achieving global controllability and ease of implementation. The forthcoming research will primarily concentrate on improving the system's fault traversal capability. By evaluating its performance during power grid failure to investigate the instability risk and subsequently enhance the anti-disturbance performance of the system.

REFERENCES

[1] H. Chojaa, A. Derouich, O. Zamzoum, S. Mahfoud, M. Taoussi, H. Albalawi, H. Benbouhenni, and M. I. Mosaad, "A novel DPC approach for DFIG-based variable speed wind power systems using DSpace," *IEEE Access*, vol. 11, pp. 9493–9510, 2023.

[2] G.-L. Lu, C.-H. Lin, and Y.-K. Wu, "Comparison of communication-based and coordination-based frequency control schemes for HVdc-connected offshore wind farms," *IEEE Trans. Ind. Appl.*, vol. 57, no. 4, pp. 3352–3365, Jul. 2021.
[3] S. Yan, X. Gao, Y. Cui, H. Zhang, and Q. Yang, "Study on distributed power-collection and cascaded boosting-voltage topology and strategy for offshore DC station," *IEEE Access*, vol. 11, pp. 23586–23595, 2023.
[4] G. D. Marques and M. F. Iacchetti, "DFIG topologies for DC networks: A review on control and design features," *IEEE Trans. Power Electron.*, vol. 34, no. 2, pp. 1299–1316, Feb. 2019.
[5] R. Yang, J. Jin, Q. Zhou, S. Mu, and A. Abu-Siada, "Superconducting magnetic energy storage based DC unified power quality conditioner with advanced dual control for DC-DFIG," *J. Modern Power Syst. Clean Energy*, vol. 10, no. 5, pp. 1385–1400, Sep. 2022.
[6] A. Akhbari, M. Rahimi, and M. H. Khooban, "Various control strategies performance assessment of the DFIG wind turbine connected to a DC grid," *IET Electric Power Appl.*, vol. 17, no. 5, pp. 687–708, May 2023.
[7] H. Nian and X. Yi, "Coordinated control strategy for doubly-fed induction generator with DC connection topology," *IET Renew. Power Gener.*, vol. 9, no. 7, pp. 747–756, Sep. 2015.
[8] S. Yan, A. Zhang, H. Zhang, and J. Wang, "Control scheme for DFIG converter system based on DC transmission," *IET Electr. Power Appl.*, vol. 11, pp. 1441–1448, Sep. 2017.
[9] S. Yan, A. Zhang, H. Zhang, J. Wang, and B. Cai, "Optimized and coordinated model predictive control scheme for DFIGs with DC-based converter system," *J. Modern Power Syst. Clean Energy*, vol. 5, no. 4, pp. 620–630, Jul. 2017.
[10] S. Yan, X. Gao, Y. Lu, Y. Cui, and Y. Cai, "Study on single-loop FCS-MPC for DC-based DFIG system," *IEEE Access*, vol. 11, pp. 54006–54016, 2023.
[11] Y. Sun, S. Yan, B. Cai, and Y. Wu, "Maximum power point tracking of DFIG with DC-based converter system using coordinated feedback linearization control," *Math. Problems Eng.*, vol. 2018, pp. 1–12, Nov. 2018.
[12] A. Kasbi and A. Rahali, "MPPT performance and power quality improvement by using fractional-order adaptive backstepping control of a DFIG-based wind turbine with disturbance and uncertain parameters," *Arabian J. Sci. Eng.*, vol. 48, no. 5, pp. 6595–6614, May 2023.
[13] Q. Liu, S. Pang, and Y. Gao, "An intelligent dual-mode control strategy for extending MPPT operation interval of DFIG," *Electric Power Compon. Syst.*, vol. 48, nos. 16–17, pp. 1848–1861, 2021.
[14] S. Yan, S. Wang, B. Cai, Y. Sun, Y. Zhou, and X. Sun, "Study on a coordinated SMC strategy for DC and doubly-controlled DFIG system," in *Proc. Chin. Autom. Congr. (CAC)*, Nov. 2018, pp. 1977–1982.
[15] Y. Sun, S. Yan, B. Cai, Y. Wu, and Z. Zhang, "MPPT adaptive controller of DC-based DFIG in resistances uncertainty," *Int. J. Control, Autom. Syst.*, vol. 19, no. 8, pp. 2734–2746, Aug. 2021.
[16] A. Sobhy and D. Lei, "Model-assisted active disturbance rejection controller for maximum efficiency schemes of DFIG-based wind turbines," *Int. Trans. Electr. Energy Syst.*, vol. 31, no. 11, 2021, Art. no. e13107.
[17] Y. Chang, I. Kocar, E. Farantatos, A. Haddadi, and M. Patel, "Short-circuit modeling of DFIG-based wtg in sequence domain considering various fault- ride-through requirements and solutions," *IEEE Trans. Power Del.*, vol. 38, no. 3, pp. 2088–2100, Jun. 2023.
[18] M. Yilmaz, R. Celikel, and A. Gundogdu, "Enhanced photovoltaic systems performance: Anti-windup pi controller in ANN-based ARV MPPT method," *IEEE Access*, vol. 11, pp. 90498–90509, 2023.
[19] Y. Ji, Z. Xu, J. Liu, and Y. Song, "Distributed extended high-gain observers for the generalized strict-feedback system," *Int. J. Robust Nonlinear Control*, vol. 33, no. 13, pp. 7649–7666, Sep. 2023.
[20] X. Cao, Q. Ge, J. Zhu, G. Kong, B. Zhang, and X. Wang, "Improved sliding mode traction control combined sliding mode disturbance observer strategy for high-speed Maglev train," *IEEE Trans. Power Electron.*, vol. 38, no. 1, pp. 827–838, Jan. 2023.
[21] H. K. Khalil, "High-gain observers in feedback control: Application to permanent magnet synchronous motors," *IEEE Control Syst. Mag.*, vol. 37, no. 3, pp. 25–41, Jun. 2017.
[22] T. Wen, Y. Liu, Q. H. Wu, and L. Qiu, "Cascaded sliding-mode observer and its applications in output feedback control part I: Observer design and stability analysis," *CSEE J. Power Energy Syst.*, vol. 7, no. 2, pp. 295–306, Mar. 2021.
[23] Z. Liu, X. Lin, Y. Gao, R. Xu, J. Wang, Y. Wang, and J. Liu, "Fixed-time sliding mode control for DC/DC buck converters with mismatched uncertainties," *IEEE Trans. Circuits Syst. I, Reg. Papers*, vol. 70, no. 1, pp. 472–480, Jan. 2023.
[24] B. Yang, Y. Hu, H. Huang, H. Shu, T. Yu, and L. Jiang, "Perturbation estimation based robust state feedback control for grid connected DFIG wind energy conversion system," *Int. J. Hydrogen Energy*, vol. 42, no. 33, pp. 20994–21005, Aug. 2017.
[25] A. Darvish Falehi, "An innovative optimal RPO-FOSMC based on multi-objective grasshopper optimization algorithm for DFIG-based wind turbine to augment MPPT and FRT capabilities," *Chaos, Solitons Fractals*, vol. 130, Jan. 2020, Art. no. 109407.
[26] Y. Liu, Q. H. Wu, X. X. Zhou, and L. Jiang, "Perturbation observer based multiloop control for the DFIG-WT in multimachine power system," *IEEE Trans. Power Syst.*, vol. 29, no. 6, pp. 2905–2915, Nov. 2014.
[27] B. Li, S. Yang, B. Yang, and K. Fang, "Robust nonlinear control of DFIG-based wind farms for damping inter-area oscillations of power systems," *Frontiers Energy Res.*, vol. 10, Jul. 2022, Art. no. 936580.
[28] B. Yang, T. Yu, H. Shu, W. Yao, and L. Jiang, "Sliding-mode perturbation observer-based sliding-mode control design for stability enhancement of multi-machine power systems," *Trans. Inst. Meas. Control*, vol. 41, no. 5, pp. 1418–1434, Mar. 2019.
[29] B. Yang, T. Yu, H. Shu, D. Zhu, N. An, Y. Sang, and L. Jiang, "Perturbation observer based fractional-order sliding-mode controller for MPPT of grid-connected PV inverters: Design and real-time implementation," *Control Eng. Pract.*, vol. 79, pp. 105–125, Oct. 2018.
[30] L. Jiang, "Nonlinear adaptive control and applications in power systems," *Fortschritte Der Physik/Progress Phys.*, vol. 45, no. 2, pp. 129–143, 2001.
[31] S. Li, T. A. Haskew, K. A. Williams, and R. P. Swatloski, "Control of DFIG wind turbine with direct-current vector control configuration," *IEEE Trans. Sustain. Energy*, vol. 3, no. 1, pp. 1–11, Jan. 2012.
[32] G. Marques and M. Iacchetti, "Overcurrent estimation in a doubly-fed induction generator-DC system during a voltage dip in the DC grid," *IET Renew. Power Gener.*, vol. 10, no. 7, pp. 1024–1032, Aug. 2016.

YULIANG SUN received the Ph.D. degree in automatic control from Qufu Normal University, Rizhao, China, in 2021. She is currently a Lecturer with the School of Engineering, Qufu Normal University. Her current research interests include wind energy conversion systems and non-linear control theory.

JINGWEI YANG received the master's degree in electronic science and technology from Beijing University of Technology, Beijing, China. From September 2013 to July 2014, he was a Visiting Scholar with the School of Electrical Engineering, Southeast University, Nanjing, China. He is currently an Associate Professor with the Department of Information Engineering, Shandong Water Conservancy Vocational College, Rizhao, China. His current research interests include power electronics and automatic control technology applications.

ZHONGCAI ZHANG (Member, IEEE) received the M.S. degree in operations research and cybernetics from Qufu Normal University, Qufu, China, in 2013, and the Ph.D. degree in control science and engineering from Southeast University, Nanjing, China, in 2016. From December 2022 to February 2023, he was a Visiting Associate Professor with the Department of Electrical and Electronic Engineering, Southern University of Science and Technology, Shenzhen, China. He is currently a Young Professor with the School of Engineering, Qufu Normal University, Rizhao, China. His current research interests include nonlinear system control, nonholonomic system control, underactuated system control, and robot applications. He serves as an Editor for *International Journal of Robotics and Control Systems*.